Multiscale Experiments and Predictive Modeling for Failure Mitigation in Additive Manufacturing of Lattices

Mattia Utzeri, Marco Sasso, Vikram S. Deshpande, and Shanmugam Kumar*

Additive Manufacturing (AM) empowers the creation of high-performance cellular materials, underscoring the increasing need for programmable and predictable energy absorption capabilities. This study evaluates the impact of a precisely tuned fused filament fabrication (FFF) process on the energy absorption and failure characteristics of 2D-thermoplastic lattice materials through multiscale experiments and predictive modeling. Macroscale in-plane compression testing of both thick- and thin-walled lattices, along with their μ-CT imaging, reveal relative density-dependent damage mechanisms and failure modes, prompting the development of a robust predictive modeling framework to capture process-induced performance variation and damage. For lower relative density lattices, an FE model based on the extended Drucker–Prager material model, incorporating Bridgman's correction with crazing failure criteria, accurately captures the crushing response. As lattice density increases, interfacial damage along bead-bead interfaces becomes predominant, necessitating the enrichment of the model with a microscale cohesive zone model to capture interfacial debonding. The predictive modeling introduces an enhancement factor, offering a straightforward method to assess the impact of the AM process on energy absorption performance, thereby facilitating the inverse design of FFF-printed lattices. This approach provides a critical evaluation of how FFF processes can be optimized to achieve the highest attainable performance and mitigate failures in architected materials.

1. Introduction

The demand for high-performance materials in industries has driven the need for sustainable solutions. Architected cellular materials are proposed as ideal candidates, as their solid parts are designed to create specific topologies that enhance mechanical or multifunctional performances while ensuring low weight[1–4] Additive Manufacturing (AM) has played a crucial role in developing innovative cellular materials across length scales, overcoming the limitations of traditional manufacturing technologies and allowing for free-shape design.[5–7] Combining the advantages of AM with high-performance materials has led to cutting-edge applications, including lattices with enhanced structural and/or multifunctional properties.[8–11] Especially, if energy absorption is the main feature to be ensured, the cell topology can be appropriately designed to exhibit a controllable and efficient crushing behavior.[12–16] Particularly in sectors like aerospace, biomedical, automotive, marine, and defense, there is a growing interest in these cellular materials due to their potential benefits in applications like impact absorbers or crash-worthy constructions.[17,18]

In impact applications of this nature, the design of additively manufactured cellular materials relies heavily on the mechanical and thermal characteristics of the base material. Consequently, high-performance polymers, especially Polyetherimide (PEI) like the commercially available Ultem 9085, are gaining increased attention. This polymer is typically 3D-printed using Fused Filament Fabrication (FFF) technique. Over time, Ultem 9085 has proven its efficacy in various industries due to its amorphous nature, providing excellent adhesive properties. This enables the creation of FFF-printed components with exceptional mechanical, thermal, structural, chemical, electrical, and notably fireproof performance, including flame retardancy, low toxicity, and minimal smoke emission.[19] Extant work primarily focuses on the exploration of FFF-printed PEI, with an emphasis on evaluating the influence of process parameters and deposition strategy on bulk mechanical properties, particularly under tensile and compression loading conditions.[20–22] Recent work by Fores-Garriga et al. has delved into assessing how the unit cell topology

M. Utzeri, S. Kumar
James Watt School of Engineering
University of Glasgow
Glasgow G128QQ, UK
E-mail: msv.kumar@glasgow.ac.uk

M. Utzeri, M. Sasso
Department of Industrial Engineering and Mathematical Sciences
Polytechnic University of Marche
Ancona 60131, Italy

V. S. Deshpande
Department of Engineering
University of Cambridge
Cambridge CB2 1PZ, UK

influences Young's modulus of PEI 2D and 3D cellular materials.[23,24] However, these studies have predominantly examined the linear elastic properties of PEI cellular materials through numerical, experimental, and analytical observations. Notably, the energy absorption characteristics of FFF-printed PEI cellular materials remain unexplored in current research endeavors.

Exploring the mechanics of FFF-printed cellular materials, the predominant focus in this field centers around abundant experimental investigations of mechanical performance.[13,25–27] Studies typically conduct compression tests on architected cellular materials with varying densities and unit cell topologies, evaluating how these factors influence mechanical properties and energy absorption trends. In contrast, the literature features a more limited number of numerical studies capable of predicting the compressive behavior of FFF-printed cellular materials. These numerical analyses focus on validating FE models applied to lattice structures with various cell topologies. The emphasis is on a specific case of relative density that ensures the robust structural integrity of lattice structures.[27,28] Significantly, there has been a noticeable increase in modeling efforts over the years, corresponding to the maturation of the FFF process. This progress plays a crucial role in elevating the quality of structures printed through FFF, resulting in finely tuned AM lattice materials with minimal variation in mechanical properties. However, challenges arise in establishing a predictive capability for AM-enabled cellular materials and structures using traditional physics-based modeling approaches such as FEM. This is due to the introduction of stochastic/random and systematic/determinate errors inherent in AM processes.

Stochastic errors, stemming from random variations and uncertainties in AM processes, prove challenging to eliminate. Nonetheless, they can be mitigated through process optimization, feedstock, and quality control via advanced monitoring and sensing, as well as through modeling and simulation. In contrast, dealing with systematic errors poses a challenge for traditional FEM, hindering the development of a reliable predictive capability. Consequently, recent efforts have shifted toward data-driven mechanics and manufacturing, aiming to develop Artificial Intelligence (AI) and Machine Learning (ML) tools capable of predicting and optimizing the performance of both ordered and disordered cellular materials.[29,30] A recent study by Maurizi et al. utilized an ML-based approach to inversely design lattices with superior buckling performance.[31] While AI and ML tools require substantial data, they may sometimes yield ill-posed or non-physical solutions as they lack a foundation in physics. To address this limitation, recent studies have focused on physics-guided ML tools for predicting and inversely designing AM-enabled lattices.[32,33] For instance, Ha et al. explored inverse design leveraging machine learning to potentially streamline design-manufacturing cycles.[34] In contrast, our study further advances physics-based modeling for the predictive analysis and inverse design of AM-enabled lattices. We posit that the nature of systematic errors lies in inter-bead damage. Consequently, we develop multiscale predictive FE models and scaling laws to evaluate the impact of a well-tuned FFF AM process on energy absorption and mitigate the failure of PEI lattices, informed by multiscale experiments and characterization.

In glassy thermoplastic polymers like PEI, extensive ductile deformation is primarily governed by shear yielding, while abrupt and brittle fractures are governed by crazing.[35,36] Consequently, the common approach in FE models involves calibrating the Drucker–Prager model, as numerous studies have examined its applicability in different polymers.[37–39] The failure criterion is typically based on the crazing mechanism, following the experimental evidence provided by Sternstein and Ongchin.[36] Contrary to expectations, FFF lattice structures are vulnerable to inter-bead damage, where beads can debond. The existing constitutive models cannot predict such failures, rendering the FE modeling approach generally incapable of providing a comprehensive predictive understanding of the mechanical response of FFF lattice structures. This limitation arises from the coupling of multiple failure modes within lattice structures (intra-layer and inter-layer) with the additive manufacturing process and unit cell sizes.[40] The cell walls of FFF-printed lattice structures, composed of 2, 3, or 4 beads, do not exhibit macroscopic homogeneity, like composite materials.[41]

Consequently, conventional debonding criteria in composite mechanics, such as Tsai-Wu, Tsai-Hill, and Puck criteria, cannot be applied. Instead, specific inter-bead failure criteria must be defined along the bead-bead interfaces through cohesive interactions.[42–44] It is essential to note that the mechanics of interfaces and interlayer bonding in FFF-printed components remain actively being explored.[40,45] A couple of recent studies utilize FE constitutive models, based on homogenization techniques, to derive material behavior from microscale observations.[46,47]

Nevertheless, selecting the most suitable additively manufactured lattice structure for industrial applications requires defining programmable mechanical performances through predictive modeling.[14,48] After establishing printing parameters, predicting the mechanical properties of lattice structures becomes crucial, considering the effects of the FFF process. Consequently, this study aims to offer a thorough assessment of the FFF process's impact on the mechanics and energy absorption performances of lattice structures through FE modeling and predictive scaling law approaches. Ultem 9085 has been chosen as the base material due to its significance in both industrial and academic contexts. Initially, the in-plane mechanical performance and energy absorption capacity of 3D-printed PEI lattice structures with four distinct unit cell topologies at varying relative densities (20%, 30%, and 40%) were evaluated under monotonic compression. Subsequently, the mechanical responses of FFF-printed lattice structures were analyzed through FE modeling, utilizing an extended Drucker–Prager yield criterion incorporating Bridgeman's correction parameter coupled with a crazing failure criterion. This model incorporates the mechanical properties of PEI filament, paired with a failure criterion based on maximum strain calibrated through the Finite Element Model Updating (FEMU) method, ensuring comprehensive consistency with the bulk material response. As the relative density of FFF-printed structures increased, inter-bead damage became predominant. Consequently, the model was enhanced with cohesive interaction along the interfaces of the lattice structures' bead-bead interfaces. In alignment with recent studies on microscale observation, the cohesive interaction was calibrated by leveraging a numerical multiscale approach based on micro-CT results
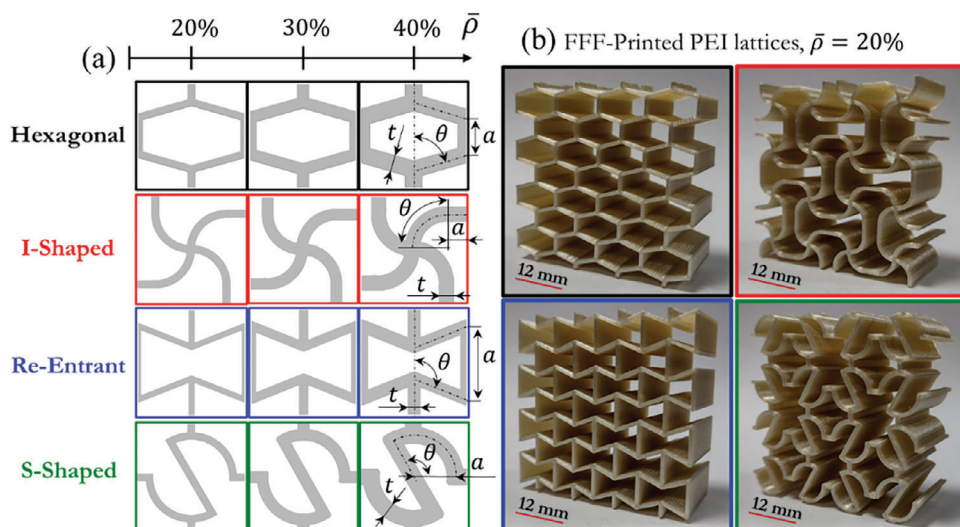
Figure 1. 2D lattice structures: a) Geometric models for different relative densities illustrating architectural parameters of various unit cell topologies and b) additively manufactured Polyetherimide (PEI) lattice structures for a relative density $\bar{\rho} = 20\%$, featuring Hexagonal (top-left), I-shaped (top-right), Re-Entrant (bottom-left), and S-shaped (bottom-right) configurations. Details of architectural parameters are summarized in Table S2 (Supporting Information).

and the Representative Volume Element of bead-bead interfaces. The final stage of predictive modeling involves introducing an enhancement factor, providing a simple scaling law to predict the energy absorption characteristics of FFF-printed structures, and estimating the impact of the FFF manufacturing process on the performance and how the FFF AM process can be tuned to mitigate failure in lattice materials.

2. Experimental Section

2.1. Additive Manufacturing of Bulk and Cellular Structures

The Apium P220 Fused Filament Fabrication (FFF) 3D printer was utilized for the fabrication of both lattice structures and fully dense samples using Polyetherimide (PEI) filament feedstocks, commonly referred to as Ultem 9085. Table S1 (Supporting Information) provides a summary of all process parameters, which have been meticulously fine-tuned through extensive testing. These parameters collectively optimized the strength, printability, and precision of geometric dimensions, ensuring the best outcomes. Consistency in printing parameters was maintained across all FFF-printed specimens to ensure uniform material properties. To prevent out-of-plane failure, a layer height of 0.1 mm was selected and the printer's nozzle was equipped with a zone heater located just above the printing surface. Before 3D printing, PEI filament was dried at 60 °C for 2 h.

PEI fully dense (bulk) samples were produced to assess the mechanical properties of FFF-printed PEI under various stress conditions, including tension, compression, bending, and triaxial loading. In all bulk samples, the infill density was set at 100% and the longitudinal direction of the bead or layer consistently aligned with the loading direction to ensure that the stress flow direction was in alignment with the orientation of the beads. The PEI lattice structures encompass four distinct unit cell topologies with three varying relative densities ($\bar{\rho}$), representing the solid volume fraction within the cellular structure, at 20%, 30%, and 40%, as illustrated in **Figure 1**. Each lattice structure has overall dimensions of 48 mm × 48 mm × 24 mm. To maintain consistent mechanical properties unaffected by boundary effects, the specimens were organized in a 4 × 4 unit cell array, following methodologies outlined in previous studies.[49,50] The unit cells maintain in-plane dimensions of 12 mm × 12 mm. To facilitate precise printing of the re-entrant lattice structure with $\bar{\rho} = 20\%$, the lowest cell wall thickness realizable was 0.8 mm. Lattice structures with higher relative densities were designed, leading to an increase in cell wall thickness while retaining the same unit cell size. The additive manufacturing process achieved this by introducing an appropriate number of beads to attain the desired size for the cell walls. Table S2 (Supporting Information) provides the architectural features for each unit cell topology. It is noteworthy that the S-shaped and I-shaped unit cells are crafted following the anti-chiral strategy, as visually demonstrated in Figure 1. All geometries were constructed using the nTopology software tool.

2.2. Experimental Procedures

2.2.1. Quasi-Static Testing

Quasi-static experiments were performed utilizing a Zwick-Roell Z050 universal testing machine. A 5 kN load cell was employed to assess the constitutive response of both 3D-printed bulk PEI material and PEI filament, while a 50 kN load cell was utilized for compression tests on cellular materials. In all cases, the tests were carried out ensuring quasi-static loading conditions, imposing a strain rate of 10^{-3} s^{-1}. The lattice structures were compressed between two cylindrical steel plates at a speed of 5 mm min^{-1}, and the entire process was recorded using a digital camera. To measure deformations in both tensile and

notched tensile tests, a 2D Digital Image Correlation technique was employed.[51]

Bulk material properties were evaluated according to ASTM standards. Tensile tests were conducted on FFF-printed dogbone-shaped specimens following ASTM D638. For evaluating flexural characteristics, Three-Point Bending (TPB) tests were performed on FFF-printed rectangular beams, following ASTM D790 guidelines. Compression tests were carried out on FFF-printed cylindrical specimens. Although the standard method (ASTM D695) originally recommended prismatic samples with a length twice their width for compression testing, this led to premature fractures due to compression instability and interlayer delamination. Consequently, a cylindrical specimen with a length equal to its diameter was preferred for these tests.[52] Triaxial properties were assessed using a notched dogbone specimen (ASTM D638) with a triaxiality factor of 0.56. For each configuration, including bulk samples, PEI filament, and cellular materials, three specimens were tested to ensure the repeatability of experimental results.

2.2.2. Differential Scanning Calorimetry (DSC)

The glass transition temperatures (T_g) were analyzed in three different scenarios: one for the PEI filament (before printing), one for the bead of the FFF-printed dogbone (post-printing), and one for the bead of the re-entrant lattice structure with relative density ($\bar{\rho}$) of 20% (post-printing). The glass transition temperatures of the beads and filament were determined using Differential Scanning Calorimetry (DSC) analysis using the DSC Seiko Exstar 6000 instrument. Samples were heated at a rate of 10 °C/min from room temperature (25 °C) to 250 °C with a constant nitrogen flow of 50 mL min^{-1}. The T_g values were calculated based on the midpoint between extrapolated heat flow.

2.2.3. Micro-Computed Tomography (μCT)

The extent of porosity and its distribution in the as-printed condition of lattice structures bulk samples were assessed through micro-computed tomography (μCT) analysis. The 2D lattice structures were scanned after the compression tests to highlight the damage mechanisms associated with in-plane crushing. The cross-sectional images of the cellular materials and bulk samples were captured using Metrotom Tomography (ZEISS) instrument, achieving a voxel size of ≈24 μm. The acquired scans were reconstructed and analyzed using Matlab software.

2.3. Multiscale Finite Element Modeling

The study involved a series of Finite Element (FE) analyses, including the validation of the mechanical behavior of both bulk (fully dense) and cellular materials and the estimation of failure parameters for both the bulk material and the bead-bead interface. Consequently, the numerical characteristics of the FE models are summarized below.

2.3.1. Dogbone FE Model

A plane-stress state was assumed to replicate the tensile response of the dogbone specimen, given its thinness and the observed planar fracture in physical tensile tests. A 4-node bilinear plane stress quadrilateral element was chosen with reduced integration and hourglass control (CPS4R). An average mesh size of 0.05 mm was utilized for the analysis.

2.3.2. Three-Point Bending (TPB) FE Model

To simulate the TPB beam's behavior, a plane-strain constraint was applied to the longitudinal section of the TPB beam due to its width being ≈12 times its thickness, thereby meeting the conditions for a plane-strain state. A 4-node bilinear quadrilateral element for plane strain analysis, featuring reduced integration and hourglass control, known as the CPE4R element, was chosen. The model was configured with a mesh size of 0.05 mm.

2.3.3. Cylindrical FE Model

To simulate the compressive response of the cylindrical sample, an axisymmetric condition was imposed. A 4-node bilinear axisymmetric quadrilateral element with reduced integration and hourglass control, referred to as the CAX4R element, was selected for the analysis. The model was created with an average mesh size of 0.05 mm.

2.3.4. Notched Dogbone FE Model

The notched dogbone-shaped specimen's FE model was constructed to capture triaxiality properties. This FE model exhibits the same numerical characteristics as the Dogbone FE model, apart from an average mesh size of 0.01 mm, particularly in proximity to the notch tip.

2.3.5. RVE-B FE Model

For the 3D FE model of the RVE-B, which includes bead-bead interfaces, an 8-node linear brick element with reduced integration and hourglass control (C3D8R) was employed for meshing. Periodic Boundary Conditions (PBCs) were applied to the external faces.[53] The overall mesh size was set at 0.01 mm, while the edges at the bead-bead interface comprised an average mesh size of 0.001 mm.

2.3.6. Lattice FE Models

The planar cross-section of each type of lattice structure was meshed using CPE4R elements due to the large width of the lattice structures ensuring a plane strain condition. To ensure at least four elements span the 0.42 mm thick bead, the mesh size was set to 0.1 mm. This strikes a balanced compromise between computational effort and the accuracy of the numerical results, as recommended in the literature.[54,55] The compressive plates were represented as rigid wires within the FE model. The wire length exceeded structure sizes to ensure uniform compression even if the structure lost its integrity. The numerical analyses on *Lattice FE models* were performed using the Abaqus/Explicit solver

**ADVANCED
SCIENCE NEWS**

www.advancedsciencenews.com

**ADVANCED
MATERIALS
TECHNOLOGIES**

www.advmattechnol.de

whereas the other FE models utilized the Abaqus/Implicit solver. The contact interactions were defined with normal and tangential contact behaviors, incorporating friction properties based on a penalty factor of 0.1 and contact separation following compression loading (hard contact). These contact interactions were applied to all surfaces, including newly created surfaces resulting from fracture.

3. Constitutive and Damage Models

3.1. Drucker–Prager Model with Bridgman's Correction (D-P Model with BC)

Constitutive models and failure criteria for glassy thermoplastic materials such as PEI or PMMA usually take into account the competition between shear-yielding and crazing.[35] To represent shear-yielding, we employ the extended Drucker–Prager yield criterion which shows substantial material ductility without fracture. To model crazing, we introduce a craze-initiation criterion based on the local maximum principal strain which depends on the local mean stress. Continuum constitutive relation for craze widening is not considered, thus the craze-breakdown and failure coincide with the craze-initiation criterion. In addition, the isotropic elastic regime before the initiation of plastic deformation was considered. After the yielding point, the work hardening was associated with the true stress–strain curve obtained from a uniaxial tensile test conducted on the PEI filament. The following sections delve into the description of the models and the calibration of the models' parameters. Note that the initially considered *D-P model* is recalled in Sections 4.2 and 4.6 to highlight its inadequacy to capture the flexural response of the parent material and compression response of lattice structures. The *D-P model* incorporates the work hardening associated with the true stress–strain curve obtained from a uniaxial compression test on an FFF-printed cylinder and the crazing failure criterion was calibrated with the ultimate failure strain measured for FFF-printed dogbone samples, as presented in Section 4.1. Therefore, the *D-P model* might be considered as the constitutive model calibrated following the traditional approach.

3.1.1. Shear-Yielding

Recent studies show that, especially for glassy thermoplastic polymers, the extended *D-P model* provides accurate prediction for determining pressure-dependent yield criterion.[38] The extended *D-P* model postulates the second invariant of the deviatoric stress tensor S_{ij}, denoted as J_2, follows a linear combination with the first invariant, I_1, of the Cauchy stress tensor σ_{ij}:

$$J_2 = A + BI_1 \tag{1}$$

where A and B are material constants and

$$I_1 = \sigma_{kk} = 3\sigma_m; \quad (k = 1, 2, 3) \tag{2}$$

$$J_2 = \frac{1}{2} S_{ij} S_{ij} \tag{3}$$

$$S_{ij} = \sigma_{ij} - \frac{\sigma_{kk}}{3} \delta_{ij} \tag{4}$$

Table 1. Calibrated parameters for extended Drucker–Prager plasticity model.

A [MPa^2]	B [MPa]	Dilation angle [deg]	Flow potential eccentricity
1466.66	−2.66	1	0.1 (Default)

where δ_{ij} is the Kronecker delta and σ_m is the mean stress. The extended *D-P* constitutive model is implemented in Abaqus. To calibrate the yield criterion, we used both uniaxial tension and compression yield strengths of FFF-printed bulk samples, presented in Section 4.1. In addition, a non-associated flow rule with the dilation angle set close to zero was chosen, ensuring incompressible inelastic deformation, thereby preserving the convexity of the yield surface and eliminating any dependency on the third deviatoric stress invariant.[27] The calibrated model parameters are listed in **Table 1**.

3.1.2. Bridgman's Correction

For FE modeling of large strain problems like the present one, it is imperative to comprehend the post-necking behavior of PEI filament to precisely capture the strain hardening and real flow curve. Therefore, the true stress–strain response of the PEI filament from the onset of necking was determined following the G'Sell approach,[56] as the filament displayed necking as evidenced by the load-displacement curve depicted in Figure 3a and Figure S1 (Supporting Information). The true stress–strain relationship was calculated up to the onset of necking (corresponding to peak load) using traditional continuum mechanics theory, given the homogeneous deformation. Beyond the peak load, the necking region experiences both radial and circumferential stresses, leading to the loss of the uniaxial stress condition. The G'Sell approach provides a framework to obtain the material's true stress–strain curve from the deformation map of the necked axisymmetric region, based on Bridgman's correction parameter. A comprehensive explanation of this procedure is provided in Section S1 (Supporting Information).
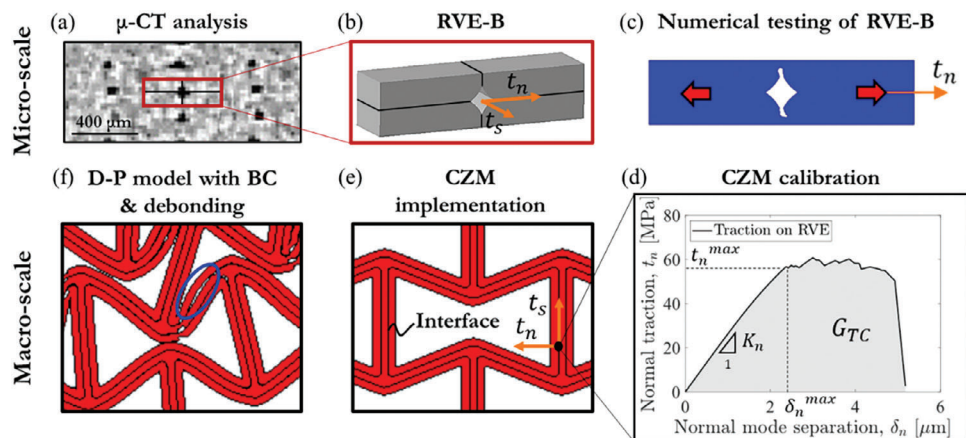
3.1.3. Crazing

Bowden and Oxborough developed an empirical crazing-initiation criterion based on critical strain,[35] given by:

$$\epsilon_1 = \frac{1}{E} \left[C(t, T) + \frac{D(t, T)}{\sigma_1 + \sigma_2 + \sigma_3} \right] \tag{5}$$

where ϵ_1 is the maximum principal strain and E is the polymer Young's modulus. σ_i denotes principal stresses (where $i = 1, 2, 3$) and both $C(t, T)$ and $D(t, T)$ are time- and temperature-dependent material constants. Assuming craze-initiation is independent of time and temperature, Equation (5) was rearranged, introducing the first invariant, I_1, of the Cauchy stress tensor σ_{ij}, as follows:

$$\epsilon_1 = X + \frac{Y}{I_1} \tag{6}$$

**ADVANCED
SCIENCE NEWS**

www.advancedsciencenews.com

**ADVANCED
MATERIALS
TECHNOLOGIES**

www.advmattechnol.de

Figure 2. Flowchart showing the steps involved in modeling the macroscale compression behavior of FFF-printed lattice structures considering inter-bead failure: a) μ-CT image showing interfaces between layers and beads topology. b) Building RVE-B from microscale observation. c) FE modeling RVE-B. d) Traction-separation response obtained from numerical tensile test on RVE-B. e) CZM implementation along bead-bead interfaces to capture inter-bead debonding. f) Debonding response predicted by *D-P model with BC & debonding*.

where *X* and *Y* are material constants. Crazing widening was considered negligible because craze-breakdown was assumed to occur at very low localized strain. To support this assumption, Gearing calibrated the complete crazing model showing a craze-breakdown strain of ≈0.005.[35] Consequently, polymer fracture can be straightforwardly modeled through Equation (6). This failure criterion was implemented in Abaqus through a user-defined subroutine utilizing the element-removal technique. The failure criterion was calibrated through inverse identification according to the Finite Element Model Updating (FEMU) method.[57] In the FEMU procedure, the dogbone (tensile) and TPB (flexural) FE models were used to simulate the real experiments. A cost function Φ (*X,Y*) is defined, which encompasses the mismatch between numerical and experimental results:

$$\Phi\ (X, Y) = \phi_D + \phi_{\mathrm{TPB}} = \left| \frac{\epsilon_f^{\mathrm{Exp}} - \epsilon_f^{\mathrm{Fem}}}{\epsilon_f^{\mathrm{Exp}}} \right| + \left| \frac{\delta_f^{\mathrm{Exp}} - \delta_f^{\mathrm{Fem}}}{\delta_f^{\mathrm{Exp}}} \right| \quad (7)$$

where ϕ_D and ϕ_{TPB} are the Normalized Root Mean Square Deviations (NRMSD) associated with tensile and flexural loading conditions, respectively. Here, $\epsilon_f^{\mathrm{Fem}}$ and $\epsilon_f^{\mathrm{Exp}}$ are the numerical
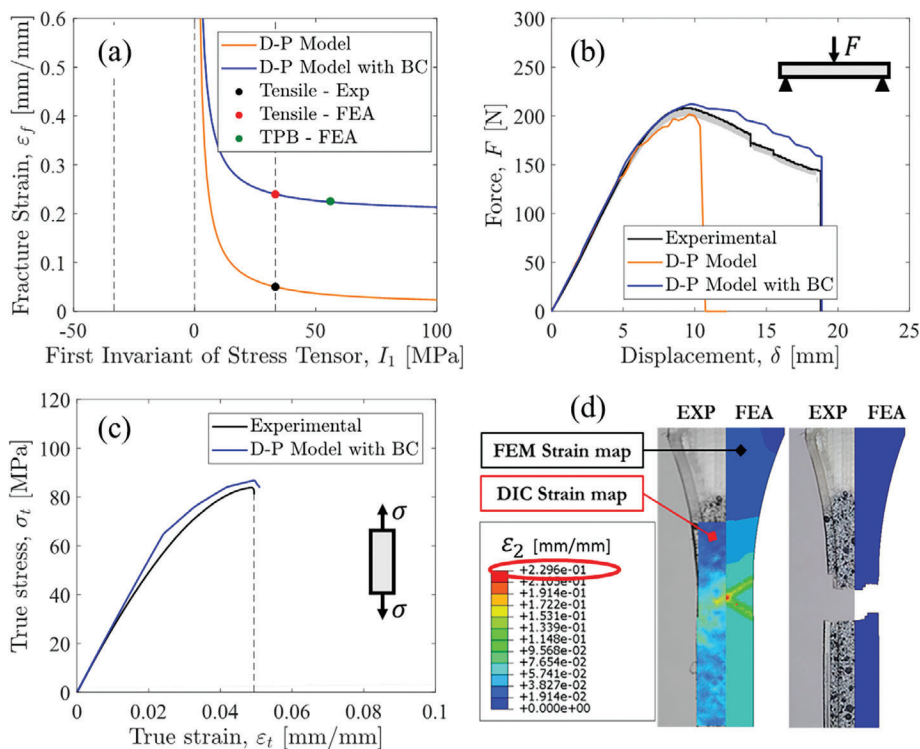
(*Dogbone FE model*) and experimental ultimate strains measured and estimated over the dogbone gauge length respectively. δ_f^{Fem} and δ_f^{Exp} are the numerical (*TPB FE model*) and experimental ultimate displacements, respectively, of the beam at the mid-span. The material constants *X* and *Y* are iteratively updated until the cost function is minimized below a given threshold. The minimization procedure was carried out using Matlab software employing the optimization solver "Fmincon". Figure S2 (Supporting Information) depicts the flowchart of the optimization procedure. The converged *X* and *Y* values by inverse identification are summarized in **Table 2** and the crazing failure criterion is graphically shown in Figure 4a.

Table 2. Calibrated parameters for crazing failure criterion.

FEA model	X [mm/mm]	Y [MPa mm/mm]
D-P model	0	1.332
D-P model with BC	0.201	1.301
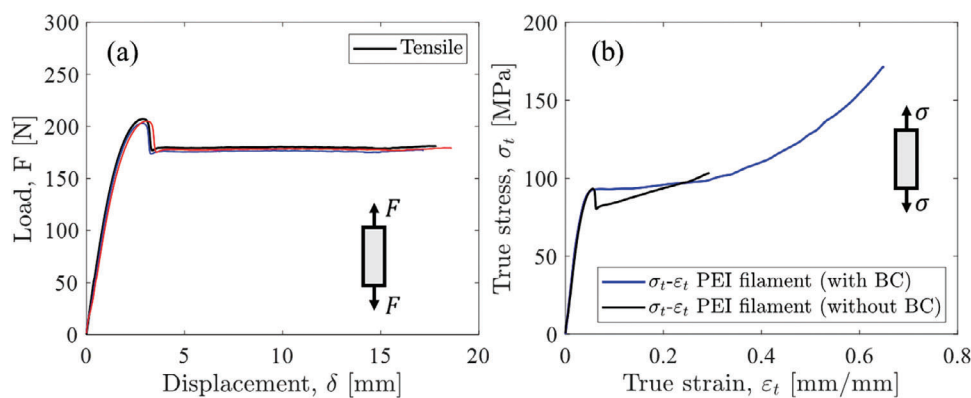
Figure 3. Quasi-static tensile response of PEI filament: a) Load–displacement behavior and b) true stress–strain curve with and without considering Bridgman's correction (BC).

ADVANCED
SCIENCE NEWS

www.advancedsciencenews.com

ADVANCED
MATERIALS
TECHNOLOGIES

www.advmattechnol.de

Figure 4. FE validation of parent material properties under tension and three-point bending (TPB). a) Crazing failure criterion calibrated in D-P model with BC and D-P model. Dots highlight the fracture strain obtained from tensile and TPB tests. b) Experimental versus numerical results of FFF-printed PEI specimen under flexural loading. c) Experimental versus numerical results of FFF-printed PEI specimen under tensile loading. d) DIC versus FEA strain maps and experimental versus FEA failures of FFF-printed PEI dogbone.

3.2. Drucker–Prager Model with Bridgman's Correction and Debonding (D-P Model with BC & Debonding)

The *D-P model with BC & Debonding* enriches the *D-P model with BC* with supplementary traction-separation cohesive law to mimic localized damage occurring along the interfaces between adjacent beads (referred to as interlayer debonding, as depicted in Figure 7). Notably, the *D-P model with BC* falls short in predicting interlayer damage, as it assumes that the cell walls are uniform and possess homogeneous properties. To capture interlayer damage, the *Lattice FE models* were updated. The planar shapes of lattice structures were subdivided based on the deposition strategy outlined in G-code instructions, forming cell walls with a specified number of beads/layers (see Figure S3, Supporting Information). The interfacial damage/fracture between beads/layers within the cell walls of the complete lattice structure is captured through a Cohesive Zone Model (CZM) described below.

3.2.1. Cohesive Zone Modeling

Cohesive Zone Modeling allows for the representation of interlaminar delamination phenomena through the establishment of a traction-separation model. Traction-separation model assumes initially linear elastic behavior defined through penalty factors K_n and K_s followed by the damage initiation and damage evolution regime. In this context, the quadratic nominal stress damage ini-

tiation criterion is employed, signifying that the bead-bead interface experiences damage when:

$$\left(\frac{\langle t_n \rangle}{t_n^{\max}}\right)^2 + \left(\frac{\langle t_s \rangle}{t_s^{\max}}\right)^2 = 1 \tag{8}$$

where the t_n is the normal traction (normal to the interface) and t_s is the in-plane shear stress. $t_n^{\max}$ and the $t_s^{\max}$ are normal and shear strengths. The damage evolution model describes the degradation of cohesive interaction using a damage variable D which evolves from 0 to 1 upon further loading after the initiation of damage:

$$t_n = \begin{cases} (1 - D)\ \bar{t}_n, & \bar{t}_n > 0 \\ \bar{t}_n, & \bar{t}_n < 0 \end{cases} \tag{9}$$

$$t_s = (1 - D)\ \bar{t}_s \tag{10}$$

where $\bar{t}_n$ and $\bar{t}_s$ are the contact stress components predicted by the elastic traction-separation behavior for the current separations without damage. The damage evolution was defined based on energy release rate and fracture toughness, so the mixed-mode criterion is implemented:

$$\frac{G_I}{G_{TC}} + \frac{G_{II}}{G_{SC}} = 1 \tag{11}$$

**ADVANCED
SCIENCE NEWS**

www.advancedsciencenews.com

**ADVANCED
MATERIALS
TECHNOLOGIES**

www.advmattechnol.de

where G_I is the energy release rate corresponding to normal traction and G_{II} is the energy corresponding to in-plane shear stress. G_{TC} and G_{SC} are the maximum fracture energy in normal traction and shear modes respectively and $G_C = G_{TC} + G_{SC}$. The damage variable D is obtained from energy information as follows:

$$D = \frac{\delta_m^f (\delta_m^{\max} - \delta_m^0)}{\delta_m^{\max} (\delta_m^f - \delta_m^0)} \tag{12}$$

where the effective separation at complete failure is $\delta_m^f = \frac{2G_c}{t_{\text{eff}}^0}$ in which t_{eff}^0 is the effective traction at damage initiation. δ_m^0 is the effective separation at damage initiation and $\delta_m^{\max}$ is the maximum value of the effective separation attained during the loading history. The traction-separation law was implemented in Abaqus as a surface-based cohesive interaction.

The cohesive model was calibrated by leveraging the Representative Volume Element (RVE) theory: the RVE for Bead interfaces (RVE-B) mimics the mechanical behavior of the bead-bead interface. Therefore, a 3D geometric model of the bead-bead interface was built from a dogbone μCT scan and then imported into Abaqus for numerical simulation (*RVE-B FE model*). The RVE-B employs the *D-P model with* BC assuming homogeneous properties inside the bead. In fact, from a microstructural point of view, amorphous polymers, like PEI, have great polymer chain diffusion, meaning polymer chains can fuse across layers exhibiting near-isotropic properties.[40] The intralayer damage was estimated based on the maximum normal and shear stresses that the RVE-B can withstand. **Figure 2** shows the flow chart and summarizes the strategy employed to predict the bead-bead interface properties.

The CZM was calibrated using the traction-separation response predicted by numerical testing on RVE-B. For example, the traction response of RVE-B depicted in Figure 2b was obtained by stretching it along the traction, t_n up to the fracture. The normal mode separation δ_n was measured as the difference between the closest fully solid cross-sections, including the porosity shape before and during the loading (see Figure S4a, Supporting Information). The normal traction was computed as the load divided by the RVE-B external area normal to t_n. The penalty factor K_n defines the slope at the early stage of traction-separation response as shown in Figure 2d, $K_n = 26\,000$ N mm^{-3}. Following Turon et al., the total fracture energy was estimated as the area under the traction-separation curve,[58] $G_{TC} = 0.22$ mJ mm^{-2}. The maximum normal traction was defined as the load at which the failure occurred, $t_n^{max} = 58$ MPa. The in-plane shear properties were defined as well: $t_s^{max} = 34$ MPa, $G_{SC} = 0.86$ mJ mm^{-2}, and $K_s = 2150$ N mm^{-3} (see Figure S4b, Supporting Information). To qualitatively assess the maximum traction and shear predictions generated by numerical testing on the RVE-B, a comparison with existing literature is conducted. The attained results reveal that the t_n^{max} is ≈70% of the bulk material strength where beads are aligned with loading direction, while the t_s^{max} accounts for ≈40% of the same benchmark. Notably, a few studies indicate that the transverse strength of bulk materials denoted here as t_n^{max}, is ≈70–80% of the tensile strength of bulk materials with beads aligned to the loading direction. Furthermore, the shear over tensile strength experiences a reduction of 50% according

to findings from various studies.[40,43,59] Consequently, the implemented numerical procedure provides reliable estimations.

4. Results and Discussion

4.1. Experiments: Mechanical Response of PEI Filament and FFF-Printed Specimens

The quasi-static mechanical behavior of the FFF-printed PEI bulk sample exhibits distinct characteristics: it displays a brittle response when subjected to tensile loading conditions (as depicted in Figure S5a, Supporting Information), whereas it shows a ductile behavior under compression loading, as shown in Figure S5b (Supporting Information). The ductility of FFF-printed PEI is further confirmed by its flexural response, as depicted in Figure S5c (Supporting Information). The compressive yield stress, σ_{CS} is estimated to be 70 MPa, while the tensile yield stress, σ_{TS} is estimated to be 62 MPa. Notably, Young's modulus in tension and compression, E_S is consistent and measures 2150 MPa. Through DIC analysis, the Poisson's ratio is determined to be 0.3596 and the fracture strain measured as the average true strain in the gauge length, ϵ_f is found to be ≈0.05. The tensile properties of FFF-printed PEI bulk materials were compared with those reported in existing literature Zaldivar et al. conducted tensile tests on Ultem 9085 dogbone samples printed horizontally to the building plate with the same layer orientation, reporting a strength of 50 MPa, Young's modulus of 2100 MPa, and a failure strain of 0.04.[20] The tensile properties observed in the present study are superior, indicating the effectiveness of process parameter selection.

The PEI filament exhibits necking, as illustrated in the load-displacement response shown in **Figure 3a** during tensile loading. This behavior is a typical trait observed in glassy thermoplastic polymers, resulting from the reorganization of polymer chains as they align along the loading direction.[56] Ultimately, the polymer undergoes brittle failure once all polymer chains are fully oriented. As detailed in the preceding section, the true stress–strain ($\sigma_t - \epsilon_t$) relationship can be determined using G'Sell's procedure (Section S1, Supporting Information for more details). Beyond the peak stress, the $\sigma_t - \epsilon_t$ relationship for the PEI filament follows a power law strain-hardening pattern as illustrated in Figure 3b, with a hardening exponent of ≈3. PEI filament exhibits a tensile strength of ≈175 MPa with a failure strain of 0.65, in stark contrast to the brittle response evidenced by the tensile test on the FFF-printed dogbone specimen.

4.2. FE Validation of PEI Bulk Properties

Before conducting FE simulations on lattice structures, the mechanical response of FFF-printed PEI specimens under tensile, compression, flexural and triaxial loading was validated, utilizing the *D-P model with BC*. It is noteworthy to highlight the FE validation of the tensile and flexural responses of 3D-printed specimens. Notably, the failure criterion in the *D-P model with BC* predicts a higher fracture strain under uniaxial tensile loading than the experimentally measured value – 0.23 versus 0.05 (red dot vs dotted vertical line in **Figure 4a,c**, respectively). Despite

**ADVANCED
SCIENCE NEWS**

www.advancedsciencenews.com

**ADVANCED
MATERIALS
TECHNOLOGIES**

www.advmattechnol.de

this apparent contradiction with the brittleness observed in FFF-printed dogbone specimens, the *D-P model with BC* accurately predicts dogbone response, confirming its effectiveness and consistency, as shown in Figure 4c. To understand the cause, attention is directed to the FE simulation. After surpassing the yielding point (Figure 4d), the FE model predicted necking, akin to the behavior of PEI filament in a tensile test, leading to a subsequent shear band. Concurrently, localized strain surpassed the fracture strain (0.23), preventing the attainment of a stable cross-section. Despite this, the average true strain within the gauge length remained ≈0.05, concealing the abrupt localization of strain. The shear band coincided with the location of the fracture in the FFF-printed dogbone specimen as shown in Figure 4d. Once failure occurred, the fracture propagated normally to the loading direction, consistent with theoretical and experimental expectations. Similar fracture behavior is commonly observed in other studies on FFF-printed dogbone specimens.[42,60] Note that if the failure strain were higher, a stable neck region would extend along the specimen's axis, mirroring the behavior observed with the PEI filament.

Figure 4b compares FE predictions with experimental results from the TBP test. The experimental data highlights a significant mismatch in mid-span displacement, denoted as δ, in stark contrast with *D-P model*. This discrepancy arises because *D-P model* was calibrated using the ultimate strain exhibited by the dogbone sample, specifically the average true strain in the gauge length (0.05). *D-P model with BC* rectifies this issue and accurately replicates the experimental observations. It can be concluded that FEMU provides ϵ_f values aligning with experimental data and effectively captures the ductility of FFF-printed PEI, previously concealed by shear banding in dogbone specimens. Furthermore, the *D-P model with BC* also validates notched tensile and compression tests, aligning well with the experimental results, as displayed in Figures S6 and S7 (Supporting Information).

4.3. Differential Scanning Calorimetry Analysis

The Differential Scanning Calorimetry (DSC) analysis, as illustrated in Figure S8 (Supporting Information), indicates that the glass transition temperature, T_g of the PEI filament is ≈181.2 °C, a value consistent with Ultem 9085. There were no significant differences in T_g between the beads forming the lattice structure and the dogbone, both measuring at ≈177 °C. Notably, the T_g of FFF-printed PEI decreased by ≈3% due to the FFF processing. Changes in T_g can be indicative of variations in mechanical properties. Turner demonstrated an empirical relationship between fracture strength, σ_f and molar mass, M for polymers, inspired by Flory's equation, given by the formula:[61]

$$\sigma_f = \sigma_\infty - \frac{A_s}{M} \tag{13}$$

Here σ_∞ is the polymer strength with infinite molar mass and A_s is a material constant. The molar mass is related to the polymer T_g through the Fox-Flory equation:
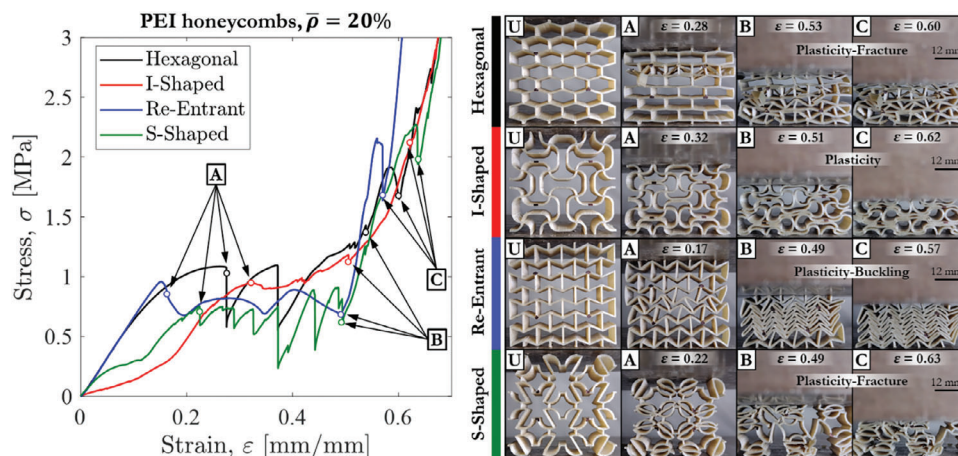
$$T_g = T_{g\infty} - \frac{B_s}{M} \tag{14}$$

where $T_{g\infty}$ is the polymer T_g with infinite molar mass and B_s is a material constant. Novikov et al. demonstrated the Fox-Flory relationship for several glassy thermoplastic polymers.[62] Given the change in T_g measured through DSC and Equations (13) and (14), it could be hypothesized that the polymer strength decreases due to FFF processing, consequently leading to a decrease in fracture strain. This observation was also confirmed by FEMU inverse identification, which validates the tensile response of FFF-printed PEI by estimating a lower fracture strain compared to the PEI filament – 0.23 versus 0.65. Therefore, it could be inferred that the FFF additive manufacturing process significantly affects the material's fracture strain, altering it from before to after the 3D printing process. On the contrary, the true stress–strain response might be assumed to resemble the filament one, as the *D-P model with BC* validates various stress states (tension, compression, flexural, and triaxial) by employing the true stress–strain curve of the PEI filament.

4.4. Experiments: Quasi-Static Compression of PEI Lattices

The in-plane compression behavior of all 3D-printed PEI 2D lattices with three different relative densities was measured under quasi-static loading conditions. The deformation and failure patterns of lattices with $\bar{\rho} = 20\%$ captured at different stages of loading along with macroscopic stress–strain response are shown in **Figure 5**: A (Initial collapse stress – σ_p), B (Onset strain of densification – ϵ_d), and C (Densification).

The stress–strain curves exhibit three well-known regimes: an initial elastic phase, a plateau regime in which lattices exhibit stable or unstable stress fluctuations, and the densification phase. The in-plane compressive response of the structures turns out to be dependent on the unit cell topology.[63] The re-entrant lattice shows a stretching-dominated behavior exhibiting an extended linear elastic regime followed by a sudden drop in stress. The re-entrant structure collapse is governed by the cell wall buckling phenomenon and extended plastic deformation which creates a stable compressive response leading to layer-by-layer collapse up to near complete densification.[64] The hexagonal, I-shaped, and S-shaped lattice structures show a bending-dominated behavior, exhibiting a nonlinear elastic regime followed by fractures or extended plastic deformation. Specifically, the hexagonal lattice structure exhibits an elastic regime followed by layer-by-layer collapse, forming crush bands and ensuring high plateau stress. The auxetic I-shaped and S-shaped lattice structures show a strong nonlinear elastic response because of the formation of additional load transfer paths between adjacent cell walls, as shown in Figure 5 (see, stage A). Note that the S-shaped structure shows a transition from a bending-dominated to a stretching-dominated mechanical response once the ligaments are completely packed. The fracture of vertical and horizontal struts which connect the "S" shaped features leads to a brittle crushing behavior in the plateau regime typical of stretch-dominated structures.[63] On the contrary, the local rotation of the ligaments in the I-shaped structure turns out to be less critical than the S-shaped structure, giving it a stable compressive response in the plateau regime and leading to smooth densification.

**ADVANCED
SCIENCE NEWS**

www.advancedsciencenews.com

**ADVANCED
MATERIALS
TECHNOLOGIES**

www.advmattechnol.de

Figure 5. In-plane quasi-static compression behavior of PEI 2D lattices with $\bar{\rho}$= 20%. Characteristic engineering stress–strain response and deformation maps at various stages including failure modes are shown: U (Undeformed), A (Initial collapse stress), B (Onset of densification), and C (Densification).

The mechanical response of PEI lattice structures changes as their relative density increases. The stress–strain curves start to exhibit a progressive brittle crushing regime dominated by ligament fractures and preferential damage along the bead-bead interfaces, i.e., interlayer damage (inter-bead debonding) as shown in Figure 7. Such a mechanical response is evident in **Figure 6** in which the in-plane quasi-static compression behavior of PEI lattice structures with $\bar{\rho} = 40\%$ is shown. The interlayer/inter-bead damage is also predominant at the intermediate relative density $\bar{\rho} = 30\%$ as shown in Figure S9 (Supporting Information). The interlayer failures are quite noticeable in the hexagonal lattice structure at stage A where the initial collapse occurs due to debonding of bead-bead interfaces. As the platen compacts the structure, the debonded beads separate and warp independently reducing the integrity of cells.

The energy absorption performance of the FFF-printed lattice structures is experimentally evaluated by comparing the onset of densification strain ϵ_d, the initial collapse stresses σ_p, and the specific energy absorption (SEA) as shown in Figure S10 (Supporting Information) and **Table 3**. The σ_p is the peak stress reached by the

structure before the collapse. The energy absorbed by the lattice structure per unit volume is defined as follows:
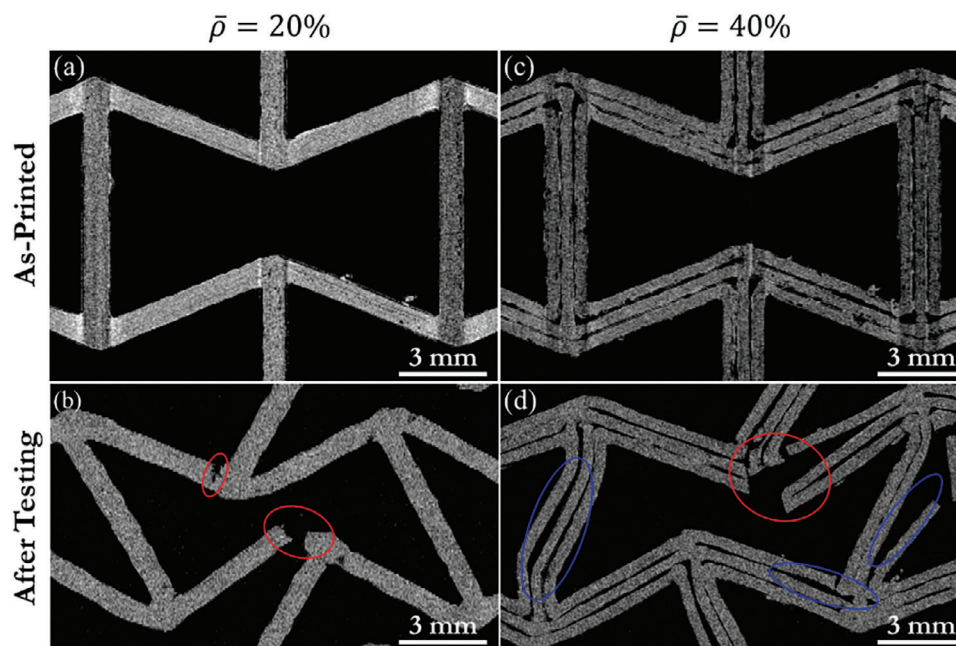
$$W = \int_0^{\epsilon_d} \sigma \, d\epsilon \tag{15}$$

and the SEA is expressed as follows:

$$SEA = \frac{W}{\rho} = \frac{1}{\rho} \int_0^{\epsilon_d} \sigma \, d\epsilon \tag{16}$$

where ρ is the average density of the lattice structure. Table 3 shows that the highest energy absorption capacity of FFF-printed structures with $\bar{\rho} = 20\%$ was achieved by the hexagonal lattice structures, including the highest σ_p and ϵ_d. Although the σ_p slightly increases as the relative density increases the SEA does not follow the same trend. That means the increase in relative density does not allow the hexagonal structure to reach higher energy absorption properties as happens for all FFF-printed structures. It is well-known that the SEA of lattice structure increases
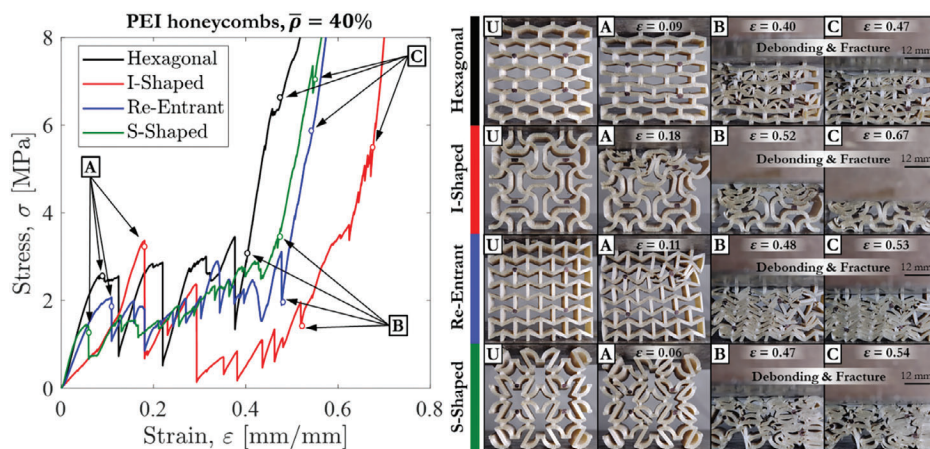
Figure 6. In-plane quasi-static compression behavior of PEI 2D lattices with $\bar{\rho} = 40\%$. Characteristic engineering stress–strain response and deformation maps at various stages including failure modes are shown: U (Undeformed), A (Initial collapse stress), B (Onset of densification), and C (Densification).

**ADVANCED
SCIENCE NEWS**

www.advancedsciencenews.com

**ADVANCED
MATERIALS
TECHNOLOGIES**

www.advmattechnol.de

Figure 7. Micro-Computed Tomography (µ-CT) analysis of re-entrant lattice structures: a) $\bar{\rho} = 20\%$ – before compression tests. b) $\bar{\rho} = 20\%$ – after compression tests, c) $\bar{\rho} = 40\%$ – before compression tests, and d) $\bar{\rho} = 40\%$ – after compression tests.

as the relative density increases in both stretching-dominated and bending-dominated lattice structures.[2,65] This correlation holds under the condition that the ligaments are defect-free, meaning they are without interlayer damage. Consequently, if there are defects present in the cell walls in their as-processed condition, the monotonic increase in SEA with the increase in relative density might not be established.
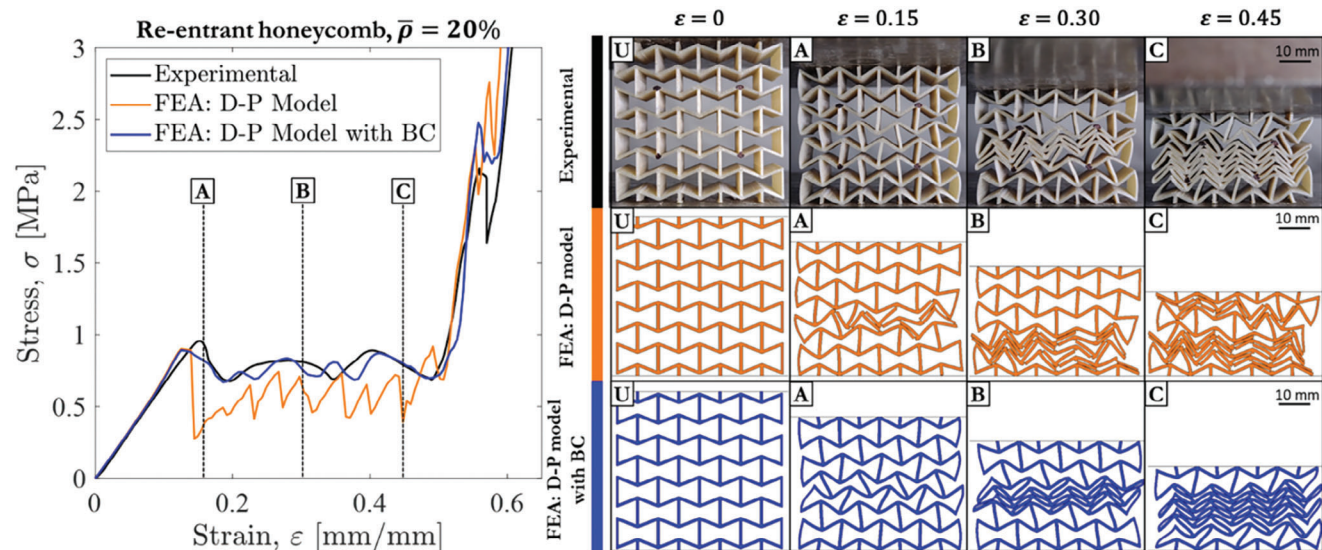
4.5. Micro-Computed Tomography Analysis

Micro-computed tomography (µCT) imaging was conducted on the lattice structures before (as-printed) and after undergoing compression tests. The re-entrant structure (as-printed) with a relative density, $\bar{\rho} = 20\%$, has no intra-bead or inter-bead micropores and defects, as illustrated in **Figure 7a**. The µCT image of the as-printed lattice structure is unable to differentiate between beads within the cell walls, where each cell wall comprises two beads, each with a thickness of 0.4 mm. This feature guarantees robust structural integrity and further validates the choice of 0.8 mm as the minimum thickness for printable cell walls. In the case of the as-printed re-entrant lattice structure with $\bar{\rho} = 40\%$, porosities were primarily observed along the bead-bead interfaces and near the cell edges, as depicted in Figure 7c. Notably, porosities were more pronounced at the interfaces between printed beads/layers than within the beads, mainly due to the elliptical cross-section of the beads, as emphasized by several studies.[40,43,66] The porosity sizes near the cell edges remained

Table 3. Summary of in-plane compression performances of FFF-printed PEI lattices.

Unit cell topology	$\bar{\rho}$ [%]	E [MPa]	ν [-]	σ_p [MPa]	ϵ_d [mm/mm]	SEA [J g^{-1}]
Hexagonal	20	7.22 ± 0.6	0.28 ± 0.01	1.09 ± 0.02	0.53 ± 0.03	2.19 ± 0.12
Hexagonal	30	22.56 ± 2.5	0.27 ± 0.02	1.28 ± 0.06	0.44 ± 0.02	1.73 ± 0.15
Hexagonal	40	41.43 ± 4.6	0.26 ± 0.02	2.63 ± 0.21	0.40 ± 0.01	2.11 ± 0.09
I-Shape	20	1.21 ± 0.3	−0.83 ± 0.02	0.96 ± 0.21	0.51 ± 0.08	1.52 ± 0.13
I-Shape	30	4.14 ± 1.2	−0.77 ± 0.03	1.84 ± 0.23	0.54 ± 0.02	2.43 ± 0.29
I-Shape	40	10.32 ± 3.4	−0.81 ± 0.02	3.34 ± 0.50	0.52 ± 0.06	1.45 ± 0.58
Re-Entrant	20	7.26 ± 0.6	−0.38 ± 0.02	0.95 ± 0.03	0.49 ± 0.03	1.67 ± 0.08
Re-Entrant	30	15.93 ± 1.8	−0.31 ± 0.01	1.91 ± 0.14	0.55 ± 0.04	2.56 ± 0.54
Re-Entrant	40	28.08 ± 4.3	−0.36 ± 0.02	2.06 ± 0.11	0.48 ± 0.02	2.06 ± 0.10
S-Shape	20	5.08 ± 0.5	−2.17 ± 0.02	0.75 ± 0.07	0.49 ± 0.01	1.27 ± 0.09
S-Shape	30	12.71 ± 1.9	−1.73 ± 0.04	1.33 ± 0.05	0.54 ± 0.05	1.81 ± 0.16
S-Shape	40	37.85 ± 3.6	−1.48 ± 0.02	1.47 ± 0.17	0.47 ± 0.04	1.99 ± 0.26

ADVANCED
SCIENCE NEWS
www.advancedsciencenews.com

ADVANCED
MATERIALS
TECHNOLOGIES
www.advmattechnol.de

Figure 8. Experimental versus FE predictions of in-plane compression behavior of re-entrant lattices with $\bar{\rho}$ = 20%. Characteristic engineering stress–strain response and deformation maps at various stages including failure modes are shown: U (Undeformed), A (ϵ = 15%), B (ϵ = 30%), and C (ϵ = 45%). (see Movie S1, Supporting Information).

consistent along the Z-direction, as it is dependent on the extrusion path. The overall structural porosity in the lattice structure, as revealed by μCT analysis, was ≈8.5%, resulting in a real relative density slightly below the intended value – 0.37 compared to the designed 0.4. The μCT analysis confirmed the accuracy of the structural dimensions, with the measured thickness of each bead at 0.41 mm compared to the designed 0.4 mm (see Figure S3, Supporting Information). This ensures that the mechanical properties obtained through experimental testing consistently pertain to a cellular material with the correct architectural parameters. Consequently, the potential for unforeseen variations in mechanical performance is predominantly associated with porosity, rather than geometric imperfections or their coexistence.

Figure 7d highlights two distinct damage mechanisms: red circles denote cracks propagating transversely to the cell walls (crazing failure), while blue ellipses highlight interlayer/inter-bead damage, specifically debonded beads within the cell walls. During compression loading, failure at the interfaces between beads leads to bead disbonding, causing warping, separation, and debonding similar to delamination in laminated materials – described as interlayer debonding. Lower-density structures do not exhibit interlayer debonding; instead, cracks propagate transversely to the beads or cell walls, as shown in Figure 7b. With increasing relative density, re-entrant structures display both damage mechanisms (see, Figure 7d) due to structural weakening at the bead-bead interfaces, as depicted in Figure 7c. Volume reconstruction shown in Figure S11 (Supporting Information) reveals no signs of out-of-plane fractures, confirming strong adhesion between stacked layers for $\bar{\rho}$ = 20% and predominant in-plane interlayer failure for $\bar{\rho}$ = 40%. This ensures the impact of the FFF process, evaluated in this study, on the mechanical performance of lattice structures is only connected to in-plane inter-bead damage. The distribution of voids within the bulk (fully dense) samples was also evaluated and presented in Figure
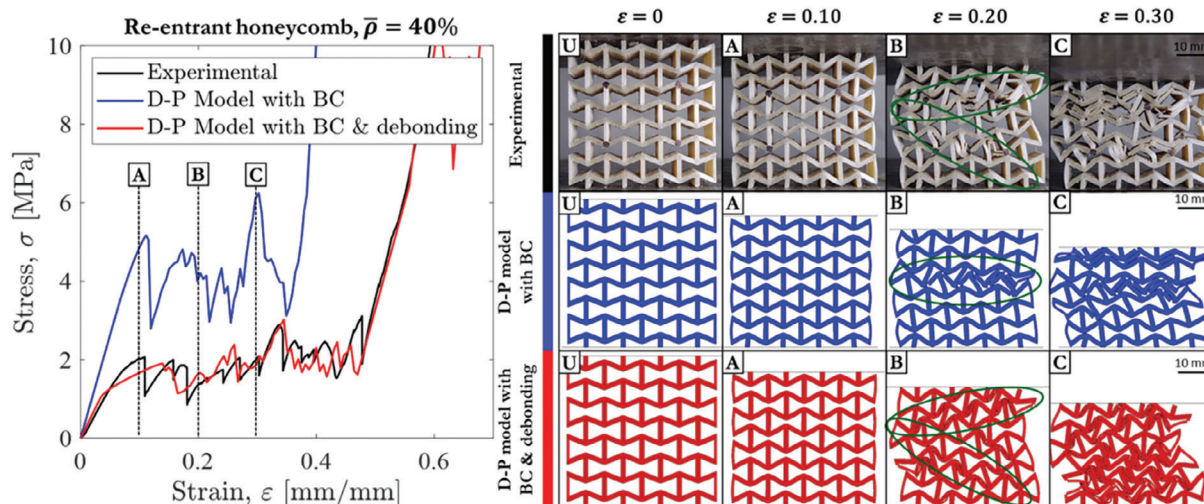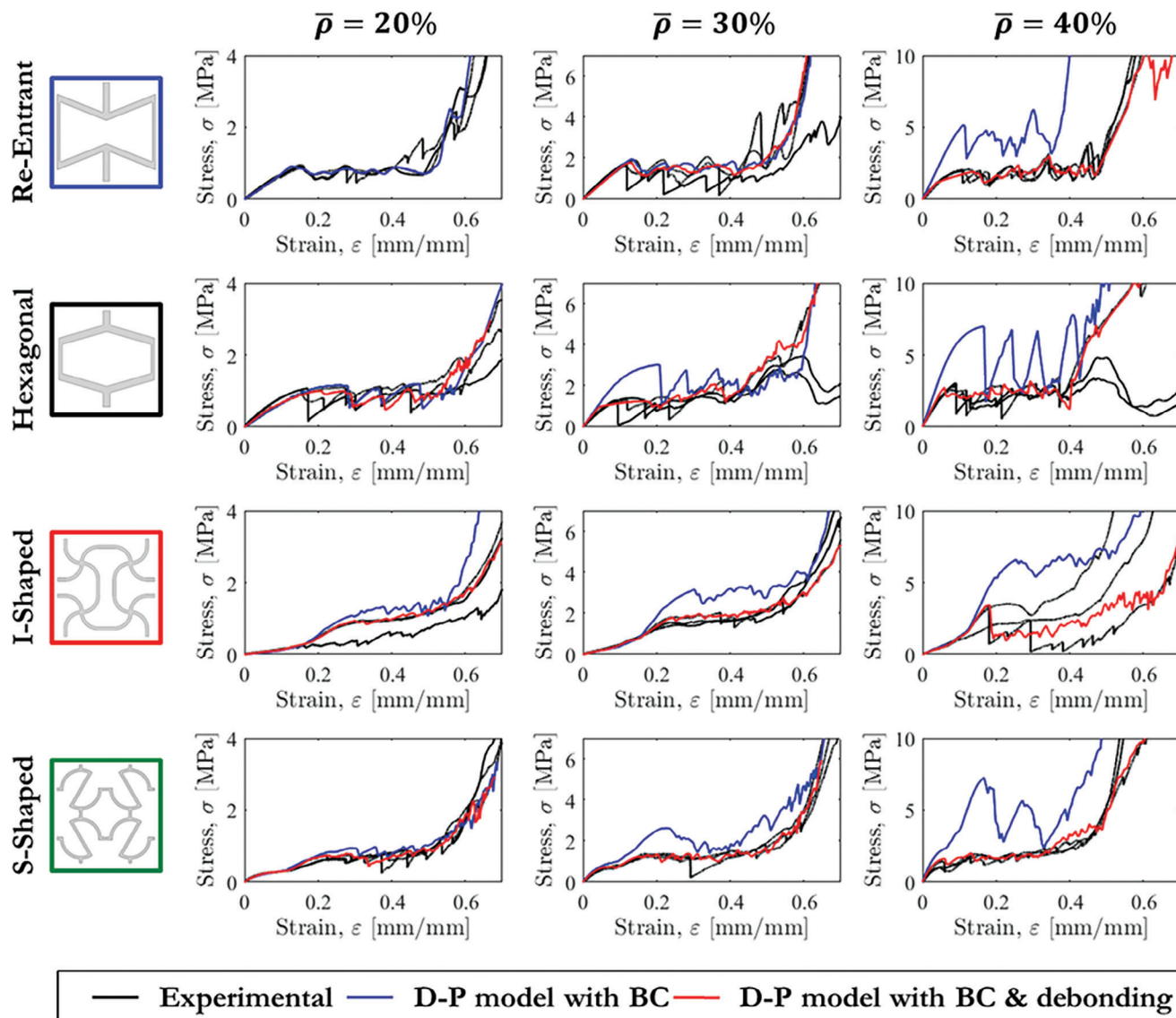
S12 (Supporting Information), with the bulk sample porosity measuring 3.6%.

4.6. FE Validation of PEI Lattice Structures

The numerical predictions of the in-plane compression behavior of re-entrant lattice structure with $\bar{\rho}$ = 20% are compared with the experimental results in **Figure 8** (see Movie S1, Supporting Information), showing the characteristic engineering stress–strain curves, deformation maps, and failures at various stages.

Both the *D-P model* and the *D-P model with BC* effectively capture the compressive response, accurately predicting the buckling phenomena of the central unit cell layer up to the initial collapse. However, the *D-P model* exhibits brittle fracture once the structure buckles (Figure 8, stage A), followed by a subsequent plateau regime governed by brittle crushing mechanisms (Figure 8, stages B and C). In contrast, the *D-P model with BC* predicts a buckled shape of a re-entrant cell that can be completely folded, mirroring the experimental test (Figure 8, stage A). The *D-P model with BC* accurately captures the layer-by-layer buckling phenomena, compacting cells without fractures in the plateau regime. The sequential buckling initiates from the central cell layer and progresses toward the cells near the compressive plates, aligning with the experimental findings observed in stages B and C. The ductility exhibited in stretched regions plays a pivotal role in the post-buckling response of the re-entrant structure, confirming the simultaneous presence of plastic yielding and elastic buckling mechanisms in the plateau regime. Consequently, the *D-P model with BC* perfectly validates the experimental compressive response of the re-entrant structure with $\bar{\rho}$ = 20%, confirming again the accuracy of the *D-P model with BC* versus the *D-P model*.

As the relative density of FFF-printed structures increases, predictions of the *D-P model with BC* become increasingly

ADVANCED
SCIENCE NEWS

www.advancedsciencenews.com

ADVANCED
MATERIALS
TECHNOLOGIES

www.advmattechnol.de

Figure 9. Experimental versus FE predictions of in-plane compression behavior of re-entrant lattices with $\bar{\rho} = 40\%$. Characteristic engineering stress–strain response and deformation maps at various stages including failure modes are shown: U (Undeformed), A ($\epsilon = 10\%$), B ($\epsilon = 20\%$), and C ($\epsilon = 30\%$). (see Movie S2, Supporting Information).

inaccurate because it cannot capture the inter-bead/interlayer debonding occurring at higher relative density as shown in **Figure 9**. The interlayer debonding changes the compressive response of the FFF-printed structures, weakening the overall mechanical performance as described in the previous section. However, the *D-P model with BC & Debonding* accurately captures the in-plane compressive response of higher relative density lattice structures as it employs a CZM to capture the interfacial damage between beads. The numerical predictions of in-plane compression behavior of re-entrant lattice structure with $\bar{\rho} = 40\%$ are compared with the experimental results in Figure 9 (see Movie S2, Supporting Information), showing the characteristic engineering stress–strain curves, deformation maps, and failures at various stages. The *D-P model with BC* predicts the buckling of the central cell layer and subsequent layer-by-layer brittle fractures (see, Figure 9 at stages B and C). On the contrary, the experimental stress–strain curve exhibits a smooth transition from the elastic to plateau regime coupled with hardening up to the first fracture, showing an initial collapse stress 2.5 times lower than that predicted by the *D-P model with BC*. Re-entrant cell buckling cannot occur at this stress level because the load is lower than the critical load required for triggering buckling instability and the initial collapse stress cannot be connected to cell buckling in turn. Structures with plateau regimes based on plastic collapse mechanisms usually exhibit similar mechanical behavior, which means inhomogeneous deformations inside the re-entrant cell walls occur.[27,49] The FFF-printed PEI material does not reach the yielding point even if thick cell walls experience a higher multi-axial stress state.[54] Thus, the inhomogeneous deformations are limited to the bead-bead interfaces, weakening the structural integrity of the re-entrant lattice structure. The macroscopic collapse response of re-entrant structure changes from layer-by-layer to diagonal (green ellipses in Figure 9 at B stage) and the *D-P model with BC & Debonding* was able to predict the macroscopic collapse. In addition, the model validates the extensive bending of the beads close to the cell edges confirming the beads' ductility. Note the change in slope from the elastic to plateau regimes

is due to the progressive failure of cohesive interaction. Once the interfaces along the structure diagonals are broken, the collapse of re-entrant cells occurs. A comparison of the predicted and experimental compressive response of hexagonal lattice structure with $\bar{\rho} = 30\%$ is provided in Section S6 and Figure S13 (Supporting Information).

4.6.1. Parametric Study

A systematic FE parametric study was conducted on all four different lattice structures with three different relative densities using both the *D-P model with BC* and the *D-P model with BC & Debonding*. A comprehensive comparison of numerical and experimental results is presented as engineering stress–strain curves in **Figure 10**. The Normalized Root Means Square Deviation (NRMSD) between experimental and numerical key mechanical attributes is summarized in Table S3 (Supporting Information). Additionally, the numerical validation of the in-plane compression behavior of PEI lattice structures is shown in Figure S14 (Supporting Information) ($\bar{\rho} = 20\%$) and Figure S15 (Supporting Information) ($\bar{\rho} = 40\%$).

The figures and Table S3 (Supporting Information) demonstrate that while the *D-P model with BC* accurately predicts the stress–strain response for lower relative density lattice structures, it fails to capture the crushing behavior of high relative density structures, exhibiting errors exceeding 100% (see Table S3, Supporting Information). In contrast, the *D-P model with BC & Debonding* accurately captures the macroscopic crushing response of all lattices tested across three different relative densities, showing consistent deformation patterns, stress–strain responses, and energy absorption characteristics with an accuracy above 90%. Although the *D-P model with BC and Debonding* does not perfectly capture all fluctuations in the post-collapse phase, it effectively models the two predominant failure mechanisms in all lattice structures: bead debonding and bead fracture. This limitation arises because the failure mechanisms in the numerical model are inherently decoupled, unlike in real-world scenarios.

**ADVANCED
SCIENCE NEWS**

www.advancedsciencenews.com

**ADVANCED
MATERIALS
TECHNOLOGIES**

www.advmattechnol.de

Figure 10. Comparison of in-plane compression behavior in PEI honeycombs: engineering stress–strain curves from experimental and numerical analyses under quasi-static compression.

In experiments, bead-bead interface fractures within cell walls tend to propagate preferentially between bead interfaces, causing debonding and locally affecting bead integrity, thereby promoting bead fractures. Despite this, the overall numerical stress–strain responses closely match experimental data, ensuring consistent results and demonstrating that inter-bead damage plays a fundamental role in the mechanical response of FFF-printed lattice materials.

4.7. Enhancement Factor

The previous section explored numerical and experimental results emphasizing the influence of interlayer damage in as-printed lattices on the in-plane compressive response of FFF-printed lattice structures. The overall mechanical performance is diminished by the interlayer damage found in lattices with high relative density. Mechanical properties, including energy absorption characteristics, generally rely on relative density. For instance, the energy absorption capacity (EAC) of lattice structures can be expressed as:

$$W = C \left(\frac{\rho}{\rho_s} \right)^{\alpha} \tag{17}$$

where C and α are topology-dependent constants.[65] The value of α for lattice structures typically ranges from 1.5 to 2, while 3D lattice structures can exhibit values up to 3.[15,64] **Figure 11a** reveals that the FFF-printed PEI lattice structures have an α parameter close to 1, indicating that the EAC of FFF-printed lattice structures deviates significantly from theoretical values. Theoretical estimate assumes defect-free cell walls: if the solid part of cellular material, like in FFF-printed structures, has inter-bead

**ADVANCED
SCIENCE NEWS**

www.advancedsciencenews.com

**ADVANCED
MATERIALS
TECHNOLOGIES**

www.advmattechnol.de
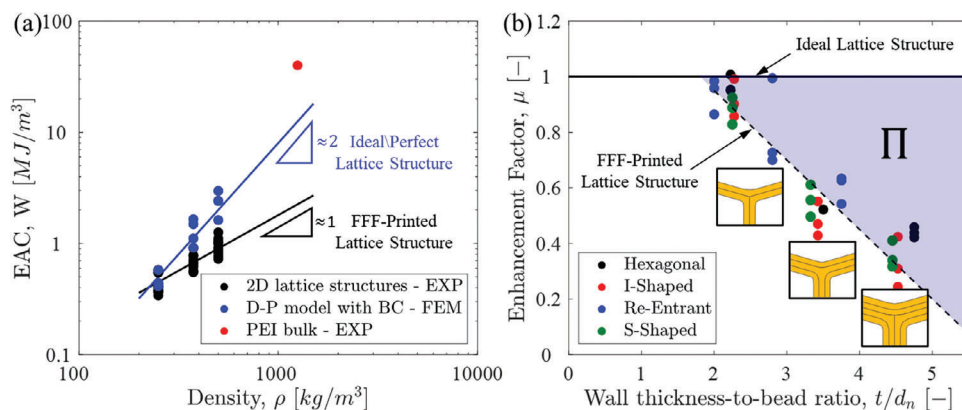
Figure 11. Impact of FFF process on energy absorption performances of PEI lattice structures. a) Influence of inter-bead damage on the energy absorption capacity of FFF-printed PEI lattice structures. b) Predictive energy absorption scaling law in FFF-printed lattice structures based on enhancement factor and wall thickness-to-bead ratio.

defects within the cell walls, Equation (17) provides a lower EAC compared to that of the same cellular structure with defect-free cell walls.

The estimation of performance decline can be achieved by introducing an enhancement factor, denoted as μ, which establishes a connection between the EAC of a perfect lattice structure and a flawed one, as per the approach outlined by Gibson and Ashby.[67] Since the interlayer damage, as well as geometric imperfections, are closely related to the FFF process, the enhancement factor μ is defined as follows:

$$\frac{W}{W^*} = \mu \tag{18}$$

Here, W represents the EAC of a lattice structure fabricated via FFF and W^* denotes the EAC of the same ideal structure, i.e., without interlayer damage. Analogously, in the context of Gibson and Ashby theory, W^* corresponds to the EAC of a perfect lattice structure. The value of W^* is obtained using the *D-P model with BC*, assuming homogeneous constitutive properties within the cell walls (absence of interlayer damage) of the lattice structure. Indeed, Figure 11a illustrates that the *D-P model with BC* predicts a relationship between W and $\bar{\rho}$ in a log-log graph according to theoretical estimate ($\alpha \simeq 2$).

The enhancement factor μ serves as a straightforward metric for assessing the impact of the AM process on EAC. However, μ must be defined as a key parameter of the FFF printing strategy, effectively linking it to the cell wall thickness to bead thickness ratio (t/d_n), where t is the cell wall thickness, and d_n is the nozzle diameter. Figure 11b demonstrates that μ decreases with an increase in t/d_n ratio, indicating a higher number of beads within the cell walls. This leads to a decline in lattice structure performance due to an elevated degree of bead-bead interfacial defects and damage. A best-fitting equation for μ is provided as:

$$\mu = -\frac{t}{4\,d_n} + 1.5 \tag{19}$$

The slope of the enhancement factor line is closely linked to process parameters, with a lower slope for the perfect lattice structure (horizontal line with a μ = 1) indicating higher in-

terlayer strength. Achieving the best performance involves minimizing the area between the dotted slant line and the solid horizontal line (representing μ = 1) in Figure 11b. In other words, reducing the shaded area denoted by Π to nearly zero results in fully solid cell walls with homogeneous material properties and intact bead-bead interfaces, indicating the highest print quality for FFF-printed structures. It is noteworthy that Habib et al. explored the mechanical properties of FFF-printed lattice structures across a range of relative densities, achieving theoretical values.[68] However, they consistently ensured the presence of two beads across the thickness of cell walls by adjusting the nozzle size, maintaining t/d_n ratio close to 2. This practice ensures the highest mechanical performance attainable by FFF-printed lattice structures and mitigates failure.

5. Conclusion

The study elucidates the effects of a meticulously tuned fused filament fabrication (FFF) additive manufacturing (AM) process on the energy absorption capabilities and failure behavior of 2D thermoplastic lattices. Employing a comprehensive approach that integrates multiscale experiments and predictive modeling, we specifically examine the in-plane crushing behavior and failure mechanisms of FFF-printed lattice structures, incorporating four distinct unit cell topologies and three relative densities. At lower relative densities, we observe anticipated bending- or stretching-dominated deformation behavior in the plateau regime. However, as relative density increases, the compressive responses undergo a shift in deformation and damage mechanisms. Low relative density structures exhibit homogeneous deformation within cell walls, while high relative density lattice structures manifest preferential damage along bead-bead interfaces (interlayer damage), as evidenced by μ-CT scans. Consequently, high relative density lattices demonstrate insufficient improvements in energy absorption performance due to their susceptibility to interlayer debonding. Our multiscale finite element models further corroborate the detrimental impact of interlayer damage on failure behavior and energy absorption performance.

The *D-P model,* initially calibrated through monoaxial tests, presents inconsistent flexural responses of the parent material and compression responses of lattice structures. As a remedy, we introduce an alternative model, the *D-P model with BC,* which accounts for the influence of the FFF process. This model utilizes the mechanical properties of PEI filament corrected by Bridgman's correction parameter and calibrates the crazing failure criteria through inverse analysis, aligning with experimental observations on FFF-printed dogbone and three-point bending specimens. Successfully capturing tensile, flexural, triaxial, and compression behaviors of FFF-printed parent material, as well as the crushing response of low relative density lattice structures, the enhanced model falls short in accurately representing the crushing response of high relative density lattice structures where inter-bead damage prevails. To address this limitation, we augment the *D-P model with BC* by introducing cohesive interactions along bead-bead interfaces (*D-P model with BC & Debonding*). This enhancement, informed by numerical simulations of a microscale RVE comprising bead-bead interfaces, effectively validates the compressive response of FFF-printed high relative density lattices and underscores the detrimental role of inter-bead damage.

In the final phase of our predictive modeling, we introduce a scaling law based on the enhancement factor and the cell wall thickness-to-bead thickness ratio. This straightforward method offers insights into the impact of the FFF AM process on the energy absorption and failure characteristics of FFF-printed lattices. The enhancement factor provides clarity on the quality of FFF-printed structures and the efficacy of chosen process parameters. Notably, maintaining a cell wall thickness-to-bead thickness ratio close to 2 proves crucial for optimal mechanical performance, steering clear of interlayer damage, and ensuring a high-quality FFF-printed structure. While intralayer damage poses challenges to the structural integrity of FFF-printed lattice structures, the introduction of the enhancement factor serves as a practical tool for predicting and evaluating the impact of FFF-3D printing on the mechanical performance and failure behavior of FFF-printed lattice structures. Moreover, the enhancement factor extends the utility of the well-established predictive scaling laws proposed by Gibson and Ashby, providing a flexible parameter for the inverse design of additively manufactured cellular materials, enhancing the adaptability and precision of the design process, and facilitating the production of defect-free lattice structures suitable for industrial adoption.

Supporting Information

Supporting Information is available from the Wiley Online Library or from the author.

Acknowledgements

Conflict of Interest

The authors declare no conflict of interest.

Data Availability Statement

The data that support the findings of this study are available in the supplementary material of this article.

Keywords

[1] N. A. Fleck, V. S. Deshpande, M. F. Ashby, *Proc. R. Soc. A* **2010**, *466*, 2495.

[2] T. A. Schaedler, W. B. Carter, *Annu. Rev. Mater. Res.* **2016**, *46*, 187.

[3] X. Zheng, H. Lee, T. H. Weisgraber, M. Shusteff, J. DeOtte, E. B. Duoss, J. D. Kuntz, M. M. Biener, Q. Ge, J. A. Jackson, S. O. Kucheyev, N. X. Fang, C. M. Spadaccini, *Science* **2014**, *344*, 1373.

[4] L. R. Meza, S. Das, J. R. Greer, *Science* **2014**, *345*, 1322.

[5] M. Kadic, G. W. Milton, M. Van Hecke, M. Wegener, *Nat. Rev. Phys.* **2019**, *1*, 198.

[6] G. Liu, X. Zhang, X. Chen, Y. He, L. Cheng, M. Huo, J. Yin, F. Hao, S. Chen, P. Wang, S. Yi, L. Wan, Z. Mao, Z. Chen, X. Wang, Z. Cao, J. Lu, *Mater. Sci. Eng.: R: Rep.* **2021**, *145*, 100596.

[7] J. Fan, L. Zhang, S. Wei, Z. Zhang, S.-K. Choi, B. Song, Y. Shi, *Mater. Today* **2021**, *50*, 303.

[8] J. Bauer, L. R. Meza, T. A. Schaedler, R. Schwaiger, X. Zheng, L. Valdevit, *Adv. Mater.* **2017**, *29*, 1701850.

[9] W. Wu, W. Hu, G. Qian, H. Liao, X. Xu, F. Berto, *Mater. Des.* **2019**, *180*, 107950.

[10] P. Verma, J. Ubaid, K. M. Varadarajan, B. L. Wardle, S. Kumar, *ACS Appl. Mater. Interfaces* **2022**, *14*, 8361.

[11] J. B. Berger, H. N. G. Wadley, R. M. McMeeking, *Nature* **2017**, *543*, 533.

[12] Z. Li, R. Zhao, X. Chen, Y. Jiao, Z. Chen, *ACS Appl. Mater. Interfaces* **2023**, *15*, 7686.

[13] J. Zhang, G. Lu, Z. You, *Composites, Part B* **2020**, *201*, 108340.

[14] Y. Wang, B. Ramirez, K. Carpenter, C. Naify, D. C. Hofmann, C. Daraio, *Extreme Mech. Lett.* **2019**, *33*, 100557.

[15] S. Yuan, C. K. Chua, K. Zhou, *Adv. Mater. Technol.* **2019**, *4*, 1800419.

[16] M.-S. Pham, C. Liu, I. Todd, J. Lertthanasarn, *Nature* **2019**, *565*, 305.

[17] M. K. Islam, P. J. Hazell, J. P. Escobedo, H. Wang, *Mater. Des.* **2021**, *205*, 109730.

2400457 (16 of 17)

[18] M. A. A. El-baky, M. M. A. Allah, M. Kamel, W. Abd-Elaziem, *Sci. Rep.* **2022**, *12*, 21097.

[19] A. Kafi, H. Wu, J. Langston, O. Atak, H. Kim, S. Kim, W. P. Fahy, R. Reber, J. Misasi, S. Bateman, J. H. Koo, *J. Appl. Polym. Sci.* **2020**, *137*, 49117.

[20] R. J. Zaldivar, D. B. Witkin, T. McLouth, D. N. Patel, K. Schmitt, J. P. Nokes, *Addit. Manuf.* **2017**, *13*, 71.

[21] A. Forés-Garriga, M. A. Pérez, G. Gómez-Gras, G. Reyes-Pozo, *Mater. Des.* **2020**, *193*, 108810.

[22] K. P. Motaparti, G. Taylor, M. C. Leu, K. Chandrashekhara, J. Castle, M. Matlack, *Virtual Phys. Prototyping* **2017**, *12*, 207.

[23] A. Forés-Garriga, G. Gómez-Gras, M. A. Pérez, *Mater. Des.* **2023**, *226*, 111641.

[24] A. Forés-Garriga, G. Gómez-Gras, M. A. Pérez, *Mater. Des.* **2022**, *215*, 110474.

[25] Y. Bian, R. Wang, F. Yang, P. Li, Y. Song, J. Feng, W. Wu, Z. Li, Y. Lu, *ACS Appl. Mater. Interfaces* **2023**, *15*, 15928.

[26] N. Kladovasilakis, K. Tsongas, I. Kostavelis, D. Tzovaras, D. Tzetzis, *Adv. Eng. Mater.* **2022**, *24*, 2100879.

[27] S. Kumar, J. Ubaid, R. Abishera, A. Schiffer, V. S. Deshpande, *ACS Appl. Mater. Interfaces* **2019**, *11*, 42549.

[28] N. K. Choudhry, B. Panda, S. Kumar, *Composites, Part B* **2022**, *228*, 109437.

[29] A. Challapalli, G. Li, *Sci. Rep.* **2021**, *11*, 18552.

[30] C. Ma, Z. Zhang, B. Luce, S. Pusateri, B. Xie, M. H. Rafiei, N. Hu, *npj Comput. Mater.* **2020**, *6*, 40.

[31] M. Maurizi, C. Gao, F. Berto, *npj Comput. Mater.* **2022**, *8*, 247.

[32] M. Abu-Mualla, J. Huang, *Mater. Des.* **2023**, *232*, 112103.

[33] B. R. Isanaka, T. Mukhopadhyay, R. K. Varma, V. Kushvaha, *Acta Mater.* **2022**, *239*, 118226.

[34] C. S. Ha, D. Yao, Z. Xu, C. Liu, H. Liu, D. Elkins, M. Kile, V. Deshpande, Z. Kong, M. Bauchy, X. Zheng, *Nat. Commun.* **2023**, *14*, 5765.

[35] B. P. Gearing, L. Anand, *Int. J. Solids Struct.* **2004**, *41*, 3125.

[36] C. B. Bucknall, *Polymer* **2007**, *48*, 1030.

[37] R. Seltzer, A. P. Cisilino, P. M. Frontini, Y.-W. Mai, *Int. J. Mech. Sci.* **2011**, *53*, 471.

[38] E. Ghorbel, *Int. J. Plasticity* **2008**, *24*, 2032.

[39] A. Pawlak, A. Galeski, *Macromolecules* **2005**, *38*, 9688.

[40] X. Gao, S. Qi, X. Kuang, Y. Su, J. Li, D. Wang, *Addit. Manuf.* **2021**, *37*, 101658.

[41] R. M. Christensen, *Compos. Sci. Technol.* **2019**, *182*, 107718.

[42] A. Sabik, M. Rucka, A. Andrzejewska, E. Wojtczak, *Mech. Mater.* **2022**, *175*, 104506.

[43] H. Gonabadi, A. Yadav, S. J. Bull, *Int. J. Adv. Manuf. Technol.* **2020**, *111*, 695.

[44] Y. Zhao, Y. Chen, Y. Zhou, *Mater. Des.* **2019**, *181*, 108089.

[45] C. McIlroy, P. D. Olmsted, *Polymer* **2017**, *123*, 376.

[46] Z. Quan, Z. Larimore, X. Qin, J. Yu, M. Mirotznik, J.-H. Byun, Y. Oh, T.-W. Chou, *Compos. Sci. Technol.* **2016**, *131*, 48.

[47] A. Nasirov, I. Fidan, *Mech. Mater.* **2020**, *145*, 103372.

[48] W. Wu, R. Xia, G. Qian, Z. Liu, N. Razavi, F. Berto, H. Gao, *Prog. Mater. Sci.* **2023**, *131*, 101021.

[49] J. J. Andrew, P. Verma, S. Kumar, *Mater. Des.* **2021**, *202*, 109516.

[50] M. F. Arif, H. Alhashmi, K. M. Varadarajan, J. H. Koo, A. J. Hart, S. Kumar, *Composites, Part B* **2020**, *184*, 107625.

[51] E. Mancini, F. Campana, D. Pilone, D. Amodio, M. Sasso, *Mater. Sci. Eng., A* **2022**, *833*, 142346.

[52] M. Utzeri, E. Farotti, M. Coccia, E. Mancini, M. Sasso, *J. Mater. Res.* **2021**, *36*, 2083.

[53] M. I. Okereke, A. I. Akpoyomare, *Comput. Mater. Sci.* **2013**, *70*, 82.

[54] W. Ronan, V. S. Deshpande, N. A. Fleck, *Int. J. Solids Struct.* **2016**, *102*, 200.

[55] E. Mancini, M. Utzeri, E. Farotti, A. Lattanzi, M. Sasso, *Mech. Mater.* **2024**, *192*, 104970.

[56] C. G'sell, N. A. Aly-Helal, J. J. Jonas, *J. Mater. Sci.* **1983**, *18*, 1731.

[57] M. Sasso, G. Newaz, D. Amodio, *Mater. Sci. Eng., A* **2008**, *487*, 289.

[58] A. Turon, C. G. Dávila, P. P. Camanho, J. Costa, *Eng. Fract. Mech.* **2007**, *74*, 1665.

[59] T. Yao, J. Ye, Z. Deng, K. Zhang, Y. Ma, H. Ouyang, *Composites, Part B* **2020**, *188*, 107894.

[60] A. Garg, A. Bhattacharya, *Int. J. Mech. Sci.* **2017**, *120*, 225.

[61] D. T. Turner, *Polymer* **1982**, *23*, 626.

[62] V. N. Novikov, E. A. Rössler, *Polymer* **2013**, *54*, 6987.

[63] J. J. Andrew, H. Alhashmi, A. Schiffer, S. Kumar, V. S. Deshpande, *Mater. Des.* **2021**, *208*, 109863.

[64] X.-T. Wang, B. Wang, X.-W. Li, L. Ma, *Int. J. Mech. Sci.* **2017**, *131–132*, 396.

[65] L. J. Gibson, M. F. Ashby, *Cellular Solids: Structure and Properties*, Cambridge University Press, Cambridge **1997**.

[66] M. F. Arif, S. Kumar, K. M. Varadarajan, W. J. Cantwell, *Mater. Des.* **2018**, *146*, 249.

[67] S. D. Papka, S. Kyriakides, *J. Mech. Phys. Solids* **1994**, *42*, 1499.

[68] F. N. Habib, P. Iovenitti, S. H. Masood, M. Nikzad, *Virtual Phys. Prototyping* **2017**, *12*, 117.